GDCh

Research Articles

Angewandte
Chemie
International Edition
www.angewandte.org

How to cite: Angew. Chem. Int. Ed. **2023**, e202315371
doi.org/10.1002/anie.202315371

Entropy-Mediated Stable Structural Evolution of Prussian White Cathodes for Long-Life Na-Ion Batteries

Yueyue He, Sören L. Dreyer, Yin-Ying Ting, Yuan Ma, Yang Hu, Damian Goonetilleke, Yushu Tang, Thomas Diemant, Bei Zhou, Piotr M. Kowalski, Maximilian Fichtner, Horst Hahn, Jasmin Aghassi-Hagmann, Torsten Brezesinski,* Ben Breitung,* and Yanjiao Ma*

Abstract: The high-entropy approach is applied to monoclinic Prussian White (PW) Na-ion cathodes to address the issue of unfavorable multilevel phase transitions upon electrochemical cycling, leading to poor stability and capacity decay. A series of Mn-based samples with up to six metal species sharing the N-coordinated positions was synthesized. The material of composition $Na_{1.65}Mn_{0.4}Fe_{0.12}Ni_{0.12}Cu_{0.12}Co_{0.12}Cd_{0.12}[Fe(CN)_6]_{0.92}\square_{0.08}\cdot1.09H_2O$ was found to exhibit superior cyclability over medium/low-entropy and conventional single-metal PWs. We also report, to our knowledge for the first time, that a high-symmetry crystal structure may be advantageous for high-entropy PWs during battery operation. Computational comparisons of the formation enthalpy demonstrate that the compositionally less complex materials are prone to phase transitions, which negatively affect cycling performance. Based on data from complementary characterization techniques, an intrinsic mechanism for the stability improvement of the disordered PW structure upon Na^+ insertion/extraction is proposed, namely the dual effect of suppression of phase transitions and mitigation of gas evolution.

Introduction

High-entropy materials (HEMs), especially the well-established high-entropy alloys (HEAs)[1] and high-entropy ceramics (HECs),[2] have been developed rapidly as functional materials that are utilized in a broad range of fields, including thermoelectricity,[3,4] environmental protection,[5] electrochemical energy storage and catalysis.[6] The emerging concept of advanced materials design based on utilizing configurational entropy to induce manifold interactions between the incorporated elements ("cocktail effect") endows the materials with unexpected and often unprecedented properties.[1,2,6,7] Introducing a large number of different elements (typically at least five) in ideally (near) equimolar proportions into a single-phase structure enables high configurational entropy, resulting in many possible interaction combinations. Several recent studies have shown that the introduction of the high-entropy concept to

[*] Y. He, S. L. Dreyer, Prof. Y. Ma, Dr. D. Goonetilleke, Dr. Y. Tang, B. Zhou, Prof. H. Hahn, Prof. J. Aghassi-Hagmann, Dr. T. Brezesinski, Dr. B. Breitung, Prof. Y. Ma
Institute of Nanotechnology, Karlsruhe Institute of Technology (KIT)
Hermann-von-Helmholtz Platz 1, 76344 Eggenstein-Leopoldshafen (Germany)
E-mail: torsten.brezesinski@kit.edu
        ben.breitung@kit.edu

Y.-Y. Ting
Institute of Energy and Climate Research (IEK-13), Forschungszentrum Jülich GmbH
Wilhelm-Johnen-Str., 52428 Jülich (Germany)

Y.-Y. Ting, Dr. P. M. Kowalski
Chair of Theory and Computation of Energy Materials, Faculty of Georesources and Materials Engineering, RWTH Aachen University
52062 Aachen (Germany)

Dr. Y. Hu, Dr. T. Diemant, Prof. M. Fichtner
Helmholtz Institute Ulm (HIU) for Electrochemical Energy Storage
Helmholtzstr. 11, 89081 Ulm (Germany)

Dr. P. M. Kowalski
Jülich Aachen Research Alliance, JARA Energy & Center for Simulation and Data Science (CSD)
52425 Jülich (Germany)

Prof. H. Hahn
School of Chemical, Biological and Materials Engineering, The University of Oklahoma
Norman, OK, 73019 (USA)

Dr. D. Goonetilleke
Current address: Corporate Research and Development, Umicore
Watertorenstraat 33, 2250 Olen (Belgium)

Prof. Y. Ma
Current address: School of Energy and Mechanical Engineering, Jiangsu Key Laboratory of New Power Batteries, Nanjing Normal University
Nanjing 210023 (China)
E-mail: yanjiao.ma@njnu.edu.cn

reversible energy storage can significantly improve cycling performance of the respective batteries. Most studies focused on materials with rock-salt type[8–10] and layered structures,[11–15] where the introduction of multiple elements into the host structure greatly affects the properties. Recently, our group reported on a novel class of battery materials, namely high-entropy metal-organic frameworks (HE-MOFs) with improved cyclability (by stabilizing the crystal structure) that can be synthesized at room temperature.[16] Several follow-up studies also confirmed the feasibility and encouraging properties of HE-MOFs,[17–21] especially their potential as insertion cathodes for next-generation batteries, such as sodium-ion batteries (SIBs). Interestingly, all of these studies focused on cubic hexacyanoferrates having five elements residing on the high-entropy site, while - to the best of our knowledge - no studies investigated MOFs with other crystalline structures and more than five elements, i.e., materials with a higher configurational entropy. Clearly, there is room to explore and expand the structural and compositional diversity of HE-MOFs for better understanding the role of configurational entropy and compositional disorder in this new materials system.

Low-cost, Mn-based Prussian White analogues ($Na_x Mn[Fe(CN)_6]$, referred to as PWs), which belong to the class of MOFs, have been demonstrated as robust host materials to enable facile Na^+ insertion/extraction in SIBs. A large number of studies have found that PWs with a low defect density, a low H_2O content and a high Na content are promising to achieving good electrochemical performance but suffer from multiple phase transitions with low-symmetry, non-cubic structures.[22–24] Apart from the rhombohedral and cubic structures,[25,26] monoclinic PWs can incorporate more sodium into the structure, making them interesting for further investigations.[27] However, they are subjected to internal structural changes and severe Jahn–Teller distortions, due to the $Mn-N_6$ octahedra experiencing large lattice strain during the uptake and removal of Na^+ ions.[27–30] It has also been reported that such monoclinic PW materials suffer from rapid capacity decay and poor reversibility caused by pronounced lattice parameter changes during the phase transitions between monoclinic $Na_2Mn[Fe(CN)_6]$, cubic $NaMn[Fe(CN)_6]$ and tetragonal $Mn[Fe(CN)_6]$.[27] Previous efforts to mitigate structural changes and improve stability of PWs mainly focused on partial atom replacements,[31–33] removal of interstitial water/vacancies,[34,35] introducing complexing agents,[36–38] forming conductive networks[39,40] or designing (cation) defect structures.[27] However, to our knowledge, the high-entropy approach has not yet been applied to low-symmetry, monoclinic PW battery materials.

In this work, we demonstrate that both the structure and cycling stability of PWs can be improved by utilizing the high-entropy approach. A six-metal high-entropy site was created at the Mn position of the conventional $Na_x Mn[Fe(CN)_6]$, forming a Mn-based HE-PW of composition $Na_{1.65}Mn_{0.4}Fe_{0.12}Ni_{0.12}Cu_{0.12}Co_{0.12}Cd_{0.12}[Fe(CN)_6]_{0.92}\square_{0.08}$. Using a combination of complementary characterizations, including electron microscopy, *operando* X-ray diffraction (XRD), *in situ* gas analysis via differential electrochemical

mass spectrometry (DEMS), X-ray photoelectron spectroscopy (XPS), X-ray absorption spectroscopy (XAS), X-ray emission spectroscopy (XES) and density functional theory (DFT) simulations, we show that an increase in configurational entropy endows the HE-PW with two positive effects, (i) strongly suppressed phase transitions and (ii) reduced gas evolution during battery operation, resulting in lower overall degradation. Compared with medium-entropy PW (ME-PW), low-entropy PW (LE-PW) and conventional single-metal PW (Mn-PW), HE-PW exhibits improved tolerance for lattice expansion and shrinkage, thereby enhancing cyclability and rate capability and contributing to a prolonged cycle life.

Results and Discussion

Structure and Composition

The crystal structure of the as-synthesized samples was investigated by XRD. The patterns of all samples, displayed in Figure S1a, revealed Bragg reflections that can be ascribed to a monoclinic structure, showing characteristic peak splitting at $2\theta \approx 10.8°–11.1°$ (−211/211), 17.1°–17.5° (031/013) and 21.7°–22.3° (42−2/422). The latter is typical of monoclinic PW materials.[27,36] Rietveld refinements were conducted to further identify the structure of the samples, and an example of the profile for the HE-PW sample is shown in Figure 1a, with corresponding structural parameters given in Table S1.

A structural model with space group $P2_1/n$ (ICSD collection code 266392/CCDC Nr. 1863351) was refined against the diffraction patterns.[41] The results show that HE-PW exhibits a monoclinic unit cell with $a = 10.476(7)$ Å, $b = 7.465(6)$ Å and $c = 7.368(6)$ Å. The local structure suggests that six metal atoms occupy the same N-coordinated (Mn) position on the 2a Wyckoff position with Mn predominating, while the C-coordinated Fe_1 atoms reside on the 2d site ($Na_x Mn[Fe_1(CN)_6]$), constituting linear chains of Fe_1-C≡N–Mn/Cd/Cu/Ni/Co/Fe_2–N≡C-Fe_1 along the monoclinic edges, as illustrated in Figure 1b. HE-PW has a very similar crystal structure (and lattice parameters) to Mn-PW, confirming the successful formation of a multielement, high-entropy site while maintaining the lattice integrity of conventional PW materials (see Figure S1b and Table S2). The chemical composition of the as-synthesized materials was analyzed by inductively coupled plasma-optical emission spectroscopy (ICP-OES), and thermogravimetric analysis (TGA) was used to determine the content of crystal water (see Table S3). The chemical formula of HE-PW was determined to be $Na_{1.65}Mn_{0.4}Fe_{0.12}Ni_{0.12}Cu_{0.12}Co_{0.12}Cd_{0.12}[Fe(CN)_6]_{0.92}\square_{0.08}\cdot 1.09H_2O$. Similar vacancy and water contents were found for all materials, ruling out any effect of vacancy/water variability on crystal structure, phase transitions and/or electrochemical performance of the HE-, ME- and LE-PW cathode materials.[35,42–44] The chemical composition as determined by ICP-OES was used to inform the site occupancies of the refined structural models discussed above. According to Equations S1 and S2 [based on the

Angew. Chem. Int. Ed. **2023**, e202315371 (2 of 14)

© 2023 The Authors. Angewandte Chemie International Edition published by Wiley-VCH GmbH
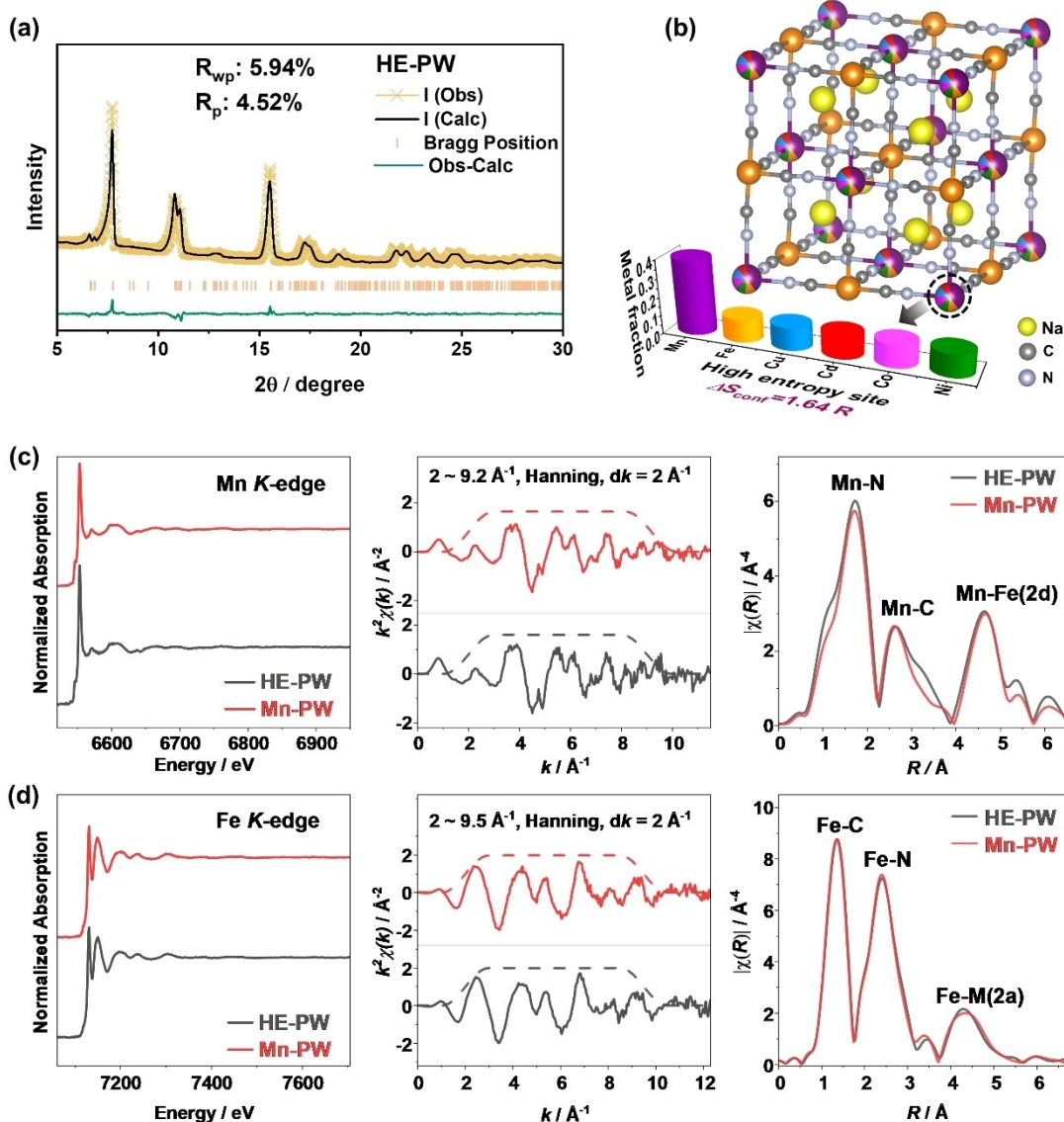
Figure 1. Structural analysis of the HE-PW and Mn-PW samples. (a) Powder XRD pattern of HE-PW and corresponding Rietveld refinement profile. (b) Schematic illustration of the crystal structure of HE-PW. (c) Mn and (d) Fe K-edge EXAFS of HE-PW and Mn-PW. Left to right: normalized absorption spectra; k^2-weighted $\chi(k)$ spectra and corresponding k range and window function (Hanging, dashed lines) for the Fourier transform; and magnitude ($|\chi(R)|$) of the Fourier-transformed, k^3-weighted $\chi(k)$.

configurational entropy (ΔS_{conf}) derived from statistical thermodynamics and introduced by Murty et al. for HEMs],[45] the ΔS_{conf} of HE-PW was calculated to be 1.64 R. Lower ΔS_{conf} values of 1.32 R and 0.82 R were obtained for ME- and LE-PW, respectively. Therefore, the formation of HE, ME and LE sites can be controlled by tailoring the composition of the Mn position in a conventional PW structure.

The local environment of the different metal ions was studied by transmission XAS. Figure 1c compares the Mn K-edge extended X-ray absorption fine structure (EXAFS) data collected from HE-PW and Mn-PW. A similar radial distribution of interatomic distances is apparent from the magnitude ($|\chi(R)|$) of the Fourier transformed, k^3-weighted $\chi(k)$, showing three distinct features corresponding to the

Mn(2a)–N, Mn(2a)–C and Mn(2a)–Fe(2d) (–CN–) coordination shells.[46] This result suggests that the Mn at the high-entropy site in HE-PW has the same coordination environment as Mn in Mn-PW, i.e., –Fe(2d)–C≡N–M(2a)–N≡C–Fe-e(2d)–. The minor differences in $|\chi(R)|$ between HE-PW and Mn-PW may result from structural and electronic modulations induced by the presence of other elements in the HE-PW. In addition, similar $|\chi(R)|$ were observed for the Fe K-edge, as the C-coordinated Fe(2d) is dominating in both the HE- and Mn-PW, evidenced by the almost identical Fe(2d)-C and Fe(2a)-N features (see Figure 1d). Moreover, synchrotron XAS (see Figure S2) revealed similar local structures for Mn, Co, Ni and Cu in the HE-PW; comparable Fourier-transformed, k^3-weighted $\chi(k)$ data were obtained, with the three main features in the $|\chi(R)|$ magnitude

corresponding to the nearest M(2*a*)-N, second M(2*a*)-C and third nearest M(2*a*)-Fe(2*d*) coordination shells.

The morphology of the materials was probed using scanning electron microscopy (SEM) and transmission electron microscopy (TEM). Micrographs collected from the HE-PW sample, see Figure 2a and b, show cubic particles having an average size of 2–3 µm. The characteristic lattice planes highlighted in the selected-area electron diffraction (SAED) pattern in Figure 2c agree with the monoclinic phase, further corroborating the $P2_1/n$ space group for HE-PW. Moreover, the high-angle annular dark-field scanning TEM (HAADF STEM) image and corresponding energy-dispersive X-ray spectroscopy (EDS) maps in Figure 2d confirm the presence of the different metal species (Na, Mn, Cd, Cu, Ni, Co and Fe). Both ME- and LE-PW were found to have a similar morphology and a relatively uniform elemental distribution on the µm level (see Figure S3).

XPS measurements were performed to determine the composition as well as the oxidation state of the different elements at the surface and to establish the initial charge compensation mechanism for the HE-PW sample. The survey spectrum (see Figure S4a) revealed the presence of the expected metal species. A single peak at a binding energy of 1071.8 eV is found in the Na 1s spectrum that can be ascribed to Na$^+$ (see Figure S4b).[16] The Mn 2p spectrum (see Figure 2e) displays major peaks at 641.4 eV (Mn 2p$_{3/2}$) and 653.1 eV (Mn 2p$_{1/2}$), accompanied by distinct satellite peaks at 646.2 and 657.9 eV. In addition, a broad Ni Auger peak appeared at ≈ 644 eV. Due to the position of the main peak doublet and because such satellite structures are typically observed for Mn^{2+} only, it can be concluded that the oxidation state of Mn is $+2$.[16] A single Cd 3d peak doublet (see Figure 2f) is detected at 405.2 eV (Cd 3d$_{5/2}$) and 411.9 eV (Cd 3d$_{3/2}$). These binding energies are typical of Cd in its preferred oxidation state $+2$, although it should be noted that the chemical shift from metallic to oxidized Cd is rather small.[47,48] The detail spectrum of the Cu 2p$_{3/2}$ region (see Figure 2g) is found to exhibit a strong peak at 932.8 eV that can be assigned to Cu$^+$.[16] A weak peak of Cu^{2+} at 935.3 eV, together with its shake-up satellite at 943.5 eV, is also detected.[8,49] The appearance of Cu$^+$ suggests that an internal redox reaction (surface reduction) from Cu^{2+} to Cu$^+$ occurred during synthesis. The Ni 2p spectrum (see Figure 2h) shows the major peak doublet at 856.2 eV (Ni 2p$_{3/2}$) and 873.7 eV (Ni 2p$_{1/2}$) and another weak doublet at slightly higher binding energies of 857.6 and 875.1 eV, as
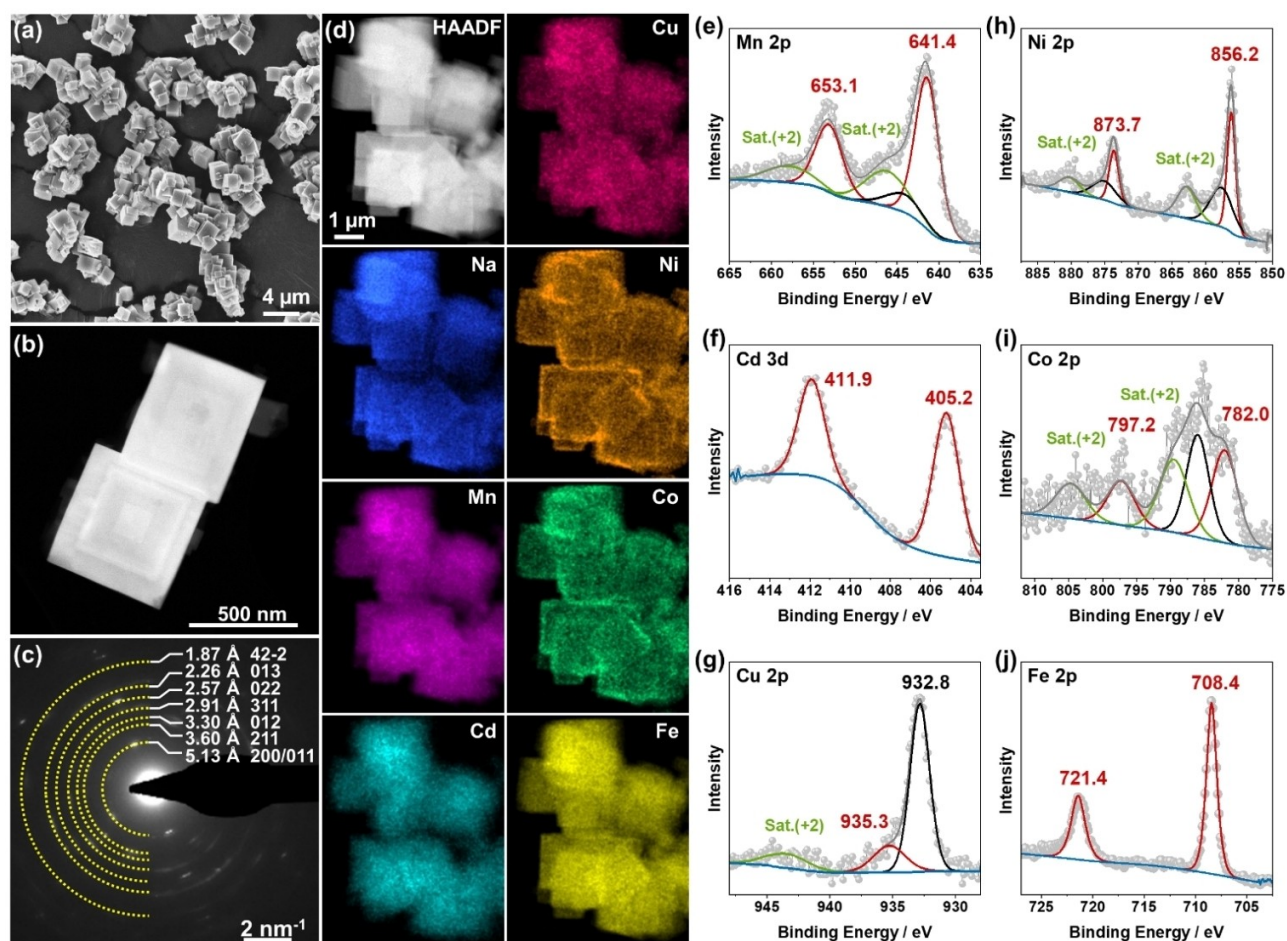
Figure 2. Electron microscopy and XPS analysis of the HE-PW sample. (a) SEM image, (b) TEM image, (c) SAED pattern, (d) HAADF STEM image and EDS elemental maps. XP spectra of the (e) Mn 2p, (f) Cd 3d, (g) Cu 2p, (h) Ni 2p, (i) Co 2p and (j) Fe 2p regions.

well as satellite features at ≈ 863 and 880 eV.[50] Evaluation of the Ni oxidation state is not possible based on these results, since the 2p binding energies are not a good measure to differentiate between different oxidation states and the peaks of oxidized Ni species reveal multiplet splitting structures. The splitting observed here could be due to the latter effect and not to the presence of different Ni oxidation states.[17] The Co 2p spectrum (see Figure 2i) shows rather distinct satellite peaks at 789.5 and 804.7 eV, together with the main peak doublet at 782.0 eV (Co $2p_{3/2}$) and 797.2 eV (Co $2p_{1/2}$) and an Fe Auger peak at ≈ 786 eV. Such satellite features are usually observed for Co^{2+}. Thus, the oxidation state of Co can also be assumed to be $+2$.[16,17] Finally, the detail spectrum of the Fe 2p region (see Figure 2j) exhibits a single peak doublet at binding energies of 708.4 eV (Fe $2p_{3/2}$) and 721.4 eV (Fe $2p_{1/2}$). This result is in agreement with

previously reported values for $[Fe^{2+}(CN)_6]^{4-}$, while the doublet of $[Fe^{3+}(CN)_6]^{3-}$ would be expected at higher binding energies ($\approx 710/723$ eV).[17] The absence of additional features seems to indicate that the free (nitrogen-coordinated) Fe ions are included in the doublet and most probably also present in $+2$ oxidation state.[37,51]

The formal oxidation states of the transition metal species were also investigated by XAS. Normalized X-ray absorption near edge structure (XANES) spectra for the respective K-edges are displayed in Figure 3. Both the HE-PW and Mn-PW showed near-edge structures similar to that of conventional PW materials.[52–54] They exhibited virtually identical Mn K-edge features, with edge energy positions close to $Mn^{2+}O$, thus indicating an oxidation state of $+2$ (see Figure 3a and Table S4). For Fe, our previous study on hexacyanoferrates revealed a mixed configuration of low-
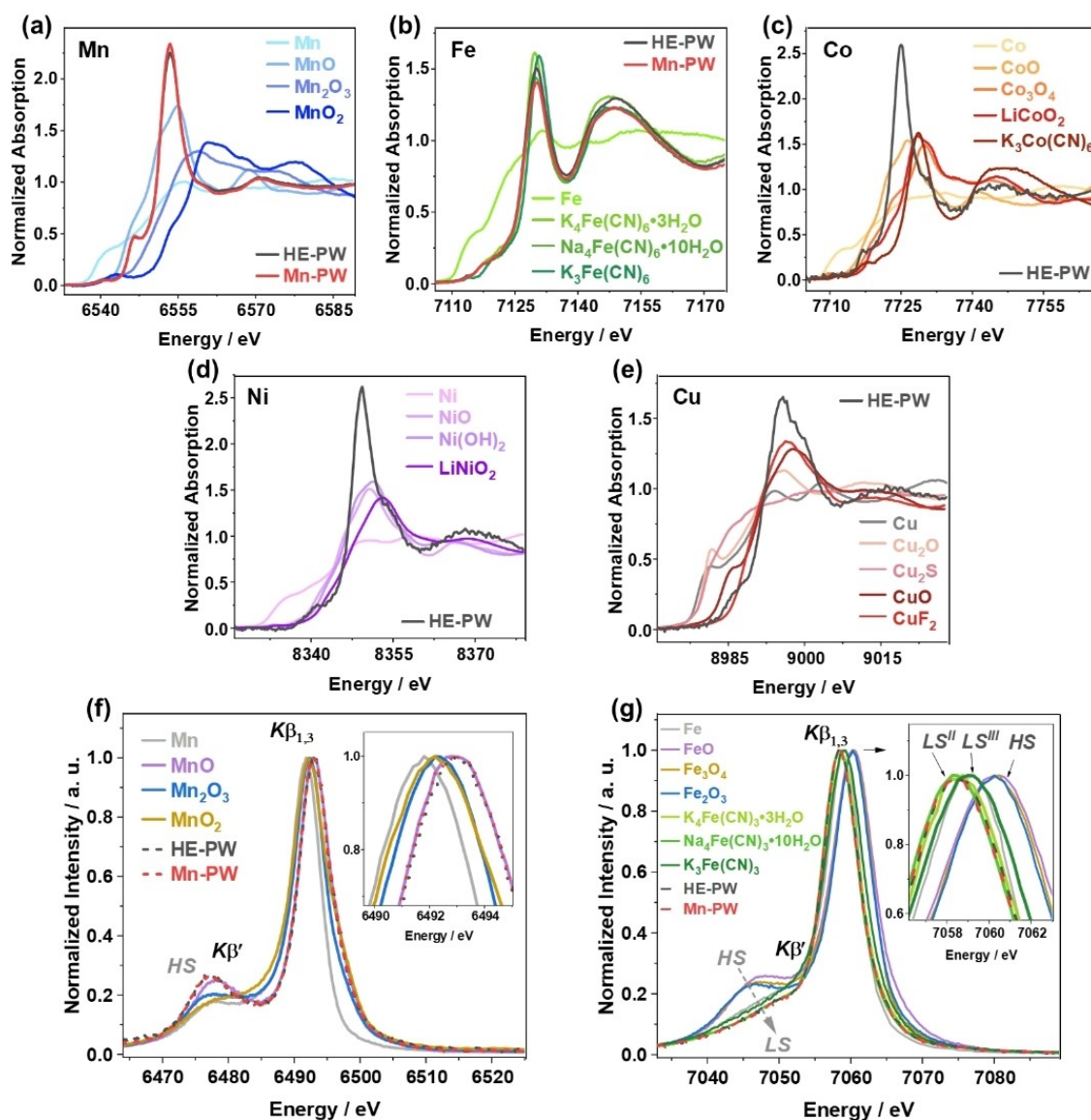
Figure 3. XANES and XES analysis of the HE-PW and Mn-PW samples. Normalized (a) Mn, (b) Fe, (c) Co, (d) Ni and (e) Cu K-edge XANES data. (f) Mn and (g) Fe $K\beta$ XES of HE-PW, Mn-PW and various reference materials. Insets show the $K\beta_{1,3}$ lines. The emission spectra were normalized by maximum peak intensity. *LS* and *HS* denote low- and high-spin configurations.

spin (LS) Fe^{2+} for the -Fe($4a$)-CN- coordination and high-spin (HS) Fe^{3+} for the -Fe($4b$)-NC- coordination,[17] with the Fe spin-state modulating the K-edge absorption. Considering the low nominal concentration (0.12 mol) of N-coordinated Fe ($2a$ Wyckoff position) in HE-PW, only reference standards with LS Fe were employed here (see Figure 3b). HE-PW and Mn-PW exhibited similar edge energy positions to $K_4Fe^{2+}(CN)_6 \cdot 3H_2O$ and $Na_4Fe^{2+}(CN)_6 \cdot 10H_2O$, which were slightly lower than that of $K_3Fe^{3+}(CN)_6$, hinting at an average (LS) Fe oxidation state of +2. On the other hand, HE-PW showed a Co K-edge with the energy position between that of $Co^{2+}O$ and $Co^{2+/3+}_3O_4$, but considerably lower compared to $K_3Co^{3+}(CN)_6$. This points toward Co^{2+} in the HE-PW sample (see Figure 3c). Similarly, the Ni and Cu K-edge spectra of HE-PW in Figure 3d and e, respectively, show edge energies close to that of $Ni^{2+}O/Ni^{2+}(OH)_2$ and $Cu^{2+}O/Cu^{2+}F_2$, again indicating an oxidation state of +2 for Ni and Cu. It should be noted that, according to XAS, the presence of Cu^+ can be ruled out. Considering the XPS results, it seems that minor amounts of Cu^+ accumulate on the surface of the material.

In addition to XANES, $K\beta$ XES was performed to probe the formal oxidation states of Mn and Fe as well as their spin states, see Figure 3f and g. The $K\beta$ emission lines of $3d$ transition metals result from a dipole-allowed $3p \rightarrow 1s$ decay process filling a core hole ($1s^1 3p^6 3d^n$) and leaving a $1s^2 3p^5 3d^n$ final state. The $3p$–$3d$ exchange coupling can lead to a $K\beta_{1,3}$/$K\beta'$ energy splitting, and the relative intensity of the $K\beta'$ feature is dependent on the number of unpaired $3d$ electrons and therefore the spin state of the respective transition metal species.[55,56] As can be seen from Figure 3f, $Mn^{2+}O$ with five unpaired $3d$ electrons ($1s^2 3p^5 t_{2g}^3 e_g^2$, $S=2.5$) showed the strongest $K\beta'$ satellite peak. With increasing oxidation state and fewer $3d$ electrons (i.e., decreasing nominal spin values) in $Mn_2^{3+}O_3$ ($1 s^2 3p^5 t_{2g}^3 e_g^1$, $S=2$) and $Mn^{4+}O_2$ ($1 s^2 3p^5 t_{2g}^3 e_g^0$, $S=1.5$), the weaker exchange interaction leads to decreased $K\beta'$ intensity and a shift of the $K\beta_{1,3}$ mainline toward lower energies.[57–59] Both the HE-PW and Mn-PW showed very similar Mn $K\beta$ XES spectra, with a strong $K\beta'$ satellite peak and the same $K\beta_{1,3}$ energy as that of MnO, providing evidence for the presence of high-spin (HS) Mn^{2+} in the -Mn($2a$)-NC- configuration. On the other hand, the Fe $K\beta$ emission lines of the hexacyanoferrates revealed very weak $K\beta'$ features, confirming the LS Fe state in the -Fe($2d$)-CN- configuration (see Figure 3g). In contrast, the oxide reference standards showed distinct satellite features, reflecting the HS Fe configuration (with oxygen ligands). Minor differences were found between HE-PW and Mn-PW, as the $K\beta$ emission lines of HE-PW are dominated by the C-coordinated, LS Fe ($2d$ Wyckoff position).[17] Both HE-PW and Mn-PW showed $K\beta'$ features identical to $K_4Fe^{2+}(CN)_6 \cdot 3H_2O$ and $Na_4Fe^{2+}(CN)_6 \cdot 10H_2O$, characteristic of the same LS Fe^{2+} ($1s^2 3p^5 t_{2g}^6 e_g^0$, $S=0$), but slightly weaker than that of $K_3Fe^{3+}(CN)_6 \cdot 3H_2O$ ($1s^2 3p^5 t_{2g}^5 e_g^0$, $S=0.5$). They also revealed $K\beta_{1,3}$ mainlines of the same energy as that of $K_4Fe^{II}(CN)_6 \cdot 3H_2O$ and $Na_4Fe^{II}(CN)_6 \cdot 10H_2O$ (slightly lower compared to $K_3Fe^{III}(CN)_6 \cdot 3H_2O$).

In summary, the Mn and Fe $K\beta$ XES data agree well with the XANES results on the average oxidation states.

The $K\beta'$ features also revealed the HS configuration of N-coordinated Mn, in addition to HS Fe on the same site, as well as the LS configuration of C-coordinated Fe. Combining the results from XPS, XAS and XES, the formal oxidation states of the C-coordinated Fe_1 and N-coordinated Mn, Cd, Cu, Ni, Co and Fe_2 (high-entropy site) are determined to be close to +2 in the monoclinic HE-PW.

Electrochemical Performance

After determining the structural and chemical properties of the PW samples and confirming successful formation of a high-entropy site, the electrochemical behavior of the HE-, ME-, LE- and Mn-PWs as SIB cathodes was examined. As shown in Figure 4a, the electrodes delivered large first-cycle specific discharge capacities of 129, 118 and 112 mAh g^{-1} for HE-PW, ME-PW and LE-PW, respectively, at 10 mA g^{-1} (126 mAh g^{-1} for Mn-PW), approaching the theoretical capacity of $\approx$130 mAh g^{-1}. Minor differences in Na content may contribute to the observed differences in the initial specific capacities. As for HE-PW, the reduced polarization (see Figure S5 and discussion below) indicates a lower overpotential, thus enabling more complete (de)sodiation at a given voltage and C-rate. A more substantial difference was observed in the long-term cycling performance, where the degree of compositional disorder appears to have a profound effect on stability, following the trend: Mn-PW < LE-PW < ME-PW < HE-PW (see Figure 4b). The capacity retention after 100 cycles was only 25 % for Mn-PW, but it increased by a factor of 1.7, 2.4 and 3.0 when using LE-PW, ME-PW and HE-PW, respectively. This is also reflected in the specific energy assuming sodium metal as the anode of a hypothetical full cell (see Figure 4c). An initial specific energy of 425 Wh kg^{-1} was achieved with the Mn-PW material, followed by a severe decay to 145 and 86 Wh kg^{-1} in the 50th and 100th cycle (only 12 % remained after 200 cycles). Figure 4c highlights the superiority of the chemically more complex materials. HE-PW was still capable of providing a specific energy of 272 and 252 Wh kg^{-1} in the 100th and 150th cycle. This is 1.4/1.5, 2.1/2.2 and 3.2/3.9 times that of ME-PW, LE-PW and Mn-PW, respectively.

Figure 4d compares the initial cyclic voltammetry (CV) curves for all PWs tested. ME-PW and LE-PW exhibited a similar behavior to conventional PW materials. Two pairs of redox peaks were found, at 3.45/3.16 V (LE-PW) and 3.50/3.10 V (ME-PW), due to redox reactions of the C-coordinated Fe^{3+}/Fe^{2+} (LS), while those at 3.65/3.32 V (LE-PW) and 3.59/3.39 V (ME-PW) can be assigned to the N-coordinated Mn^{3+}/Mn^{2+} (HS) redox couple.[17,25] With increasing ΔS_{conf}, the features merged into single broad and asymmetric peaks. Figure S5 presents CV curves collected at different sweep rates ranging from 0.05 to 2.0 mV s^{-1}. Notably, the polarization was much lower for HE-PW, especially compared to that of LE- and Mn-PW, suggesting more facile Na$^+$ insertion/extraction (potentially benefiting from the cocktail effect).[16]

The advantage of using HE-PW is also evident from the rate capability data. Figure 4e shows the performance of the
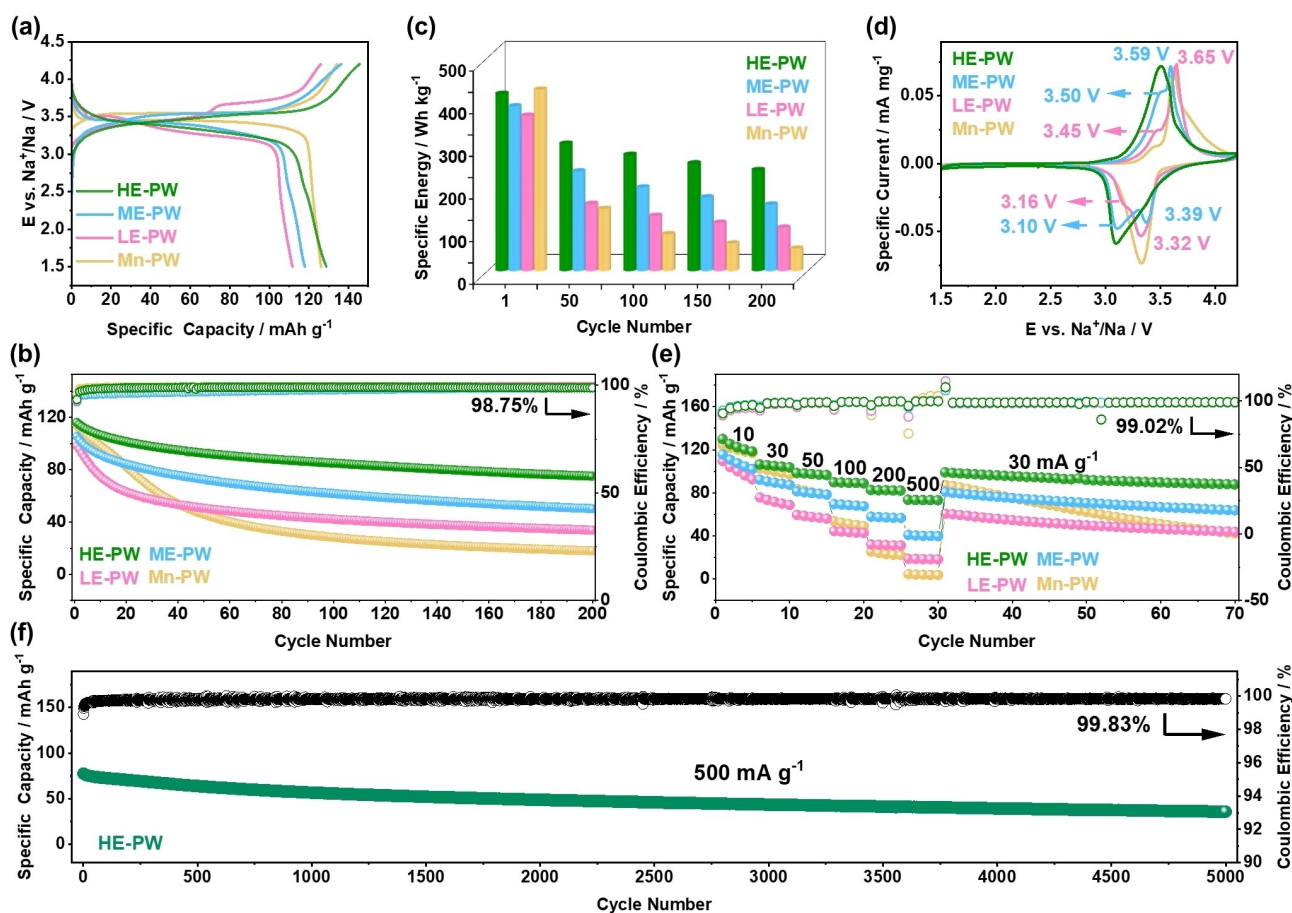
Figure 4. Electrochemical performance of the HE-, ME-, LE- and Mn-PW cathodes in SIB cells. (a) First-cycle charge/discharge curves at $10\ \mathrm{mA\,g^{-1}}$, (b) specific discharge capacity versus cycle number at $30\ \mathrm{mA\,g^{-1}}$, (c) comparison of specific energies for selected cycles, (d) initial cyclic voltammograms at $0.05\ \mathrm{mV\,s^{-1}}$, (e) rate capability for specific currents ranging from 10 to $500\ \mathrm{mA\,g^{-1}}$ and (f) long-term cycling performance of HE-PW at $500\ \mathrm{mA\,g^{-1}}$.

HE-, ME-, LE- and Mn-PW cathodes at different specific currents. HE-PW was found to deliver the largest specific discharge capacities, irrespective of the C-rate. At the highest specific current of $500\ \mathrm{mA\,g^{-1}}$, for instance, HE-PW achieved a capacity of $73\ \mathrm{mAh\,g^{-1}}$, compared to $41\ \mathrm{mAh\,g^{-1}}$ for ME-PW, $19\ \mathrm{mAh\,g^{-1}}$ for LE-PW and only $5\ \mathrm{mAh\,g^{-1}}$ for Mn-PW. Upon reducing the specific current to the initial value after rate performance testing, the capacity of HE-PW was largely recovered and remained fairly stable at $\approx100\ \mathrm{mAh\,g^{-1}}$. In contrast, rapid fading was observed in case of the Mn-PW cathode, confirming that increased ΔS_{conf} is beneficial to the reversibility of Na^+ storage. Moreover, at a high specific current of $500\ \mathrm{mA\,g^{-1}}$, the HE-PW was found to enable stable cycling for more than 5000 cycles, with $q_{\mathrm{dis}} = 60\ (\pm15)\ \mathrm{mAh\,g^{-1}}$ and the Coulomb efficiency approaching 100% (see Figure 4f). Comparative analysis with conventional (single- or dual-metal) hexacyanoferrates as cathode materials in SIBs, see Table S5, underscores the good electrochemical performance of the HE-PW sample. This result indicates that compositional disorder can be used as a means to optimize cyclability. In addition, the superiority of HE-PW, due to its robust structure, is also evident from cycling at elevated temperatures (see Figure S6). It should

be noted that the effect of configurational entropy on thermal stability of HEMs is largely unexplored and worth investigating in the future.[30]

Energy-Storage Mechanism and Entropy-Mediated Effects

Operando XRD measurements were conducted on the HE-, ME-, LE- and Mn-PW cathodes to examine the impact of the incorporated elements on crystal structure during cycling (seeking the reason for the differences in electrochemical behavior among the materials). As can be seen from Figure 5a, the Mn-PW cathode revealed multistep phase changes upon Na^+ insertion/extraction. In the beginning of charging, the reflections at around $13.2°$ and $14.2°$ [(200) and (110) crystal planes of the initial monoclinic phase] gradually shifted toward lower angles, accompanied by an expansion of the unit cell. They then merged into a single reflection situated at $13.1°$, reflecting the (200) plane of the cubic structure when charging the cell to $\approx3.55\ \mathrm{V}$. At the same time, new peaks corresponding to the (220), (400), (420) and (440) crystal planes appeared during the first phase transition from monoclinic to cubic structure. As expected,
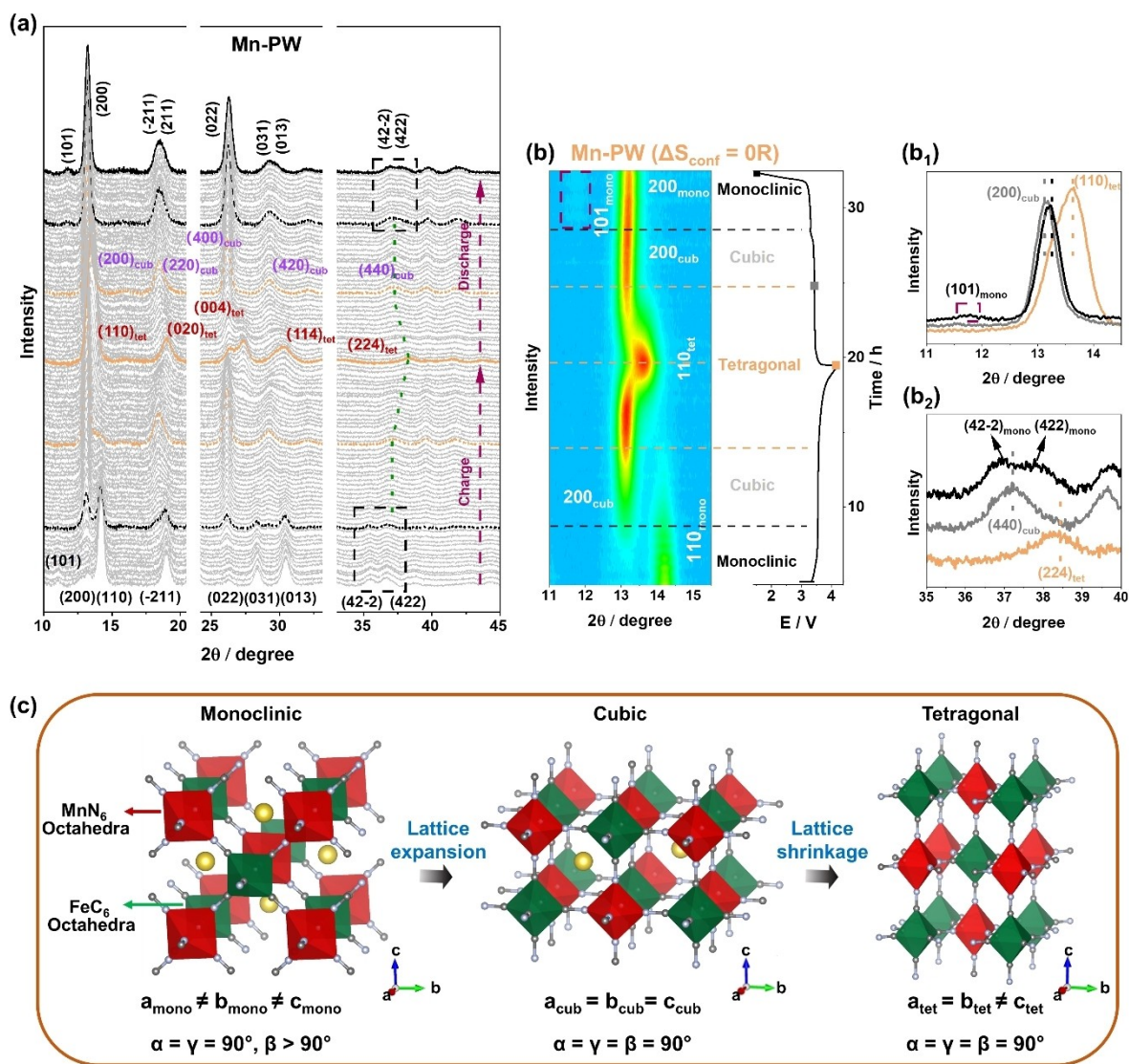
Figure 5. *Operando* XRD characterization of the Mn-PW cathode. (a) Waterfall plot (scans between 10° to 45° 2-theta). (b) Contour plot and corresponding voltage profile. (b₁, b₂) XRD patterns collected at the end of charge and during subsequent discharge [see orange, gray and black squares marked in the dis-/charge profile in panel (b)]. (c) Schematic illustration of the structural evolution of Mn-PW during battery operation.

these peaks, representing the cubic phase of Mn-PW, shifted to larger angles with increasing potential, leading to a contraction of the unit cell. New diffraction peaks associated with the (110), (020), (004), (114) and (224) planes of a tetragonal structure emerged during further charging, indicating the occurrence of a second phase transition resulting from a unit-cell deformation of the face-centered cubic structure.[27,60] In the subsequent re-sodiation process, the structure transformed back from tetragonal to cubic with discharging the cell to 3.4 V. As is evident from Figure 5b-b₂, the monoclinic phase re-appeared in the fully sodiated state, and this may lead to a decrease in the degree of crystallinity of the material (broader reflections of lower overall intensity). As also discussed in previous reports,[27,37] transitions between monoclinic, cubic and tetragonal phases during Na^+ insertion/extraction typically lead to severe (anisotropic) volume changes, meaning the Mn-PW material

suffers strongly from lattice expansion/contraction, see Figure 5c.

In contrast, the HE-PW material exhibited a more robust evolution and was able to preserve a high structural symmetry during battery operation. An initial transition from monoclinic to cubic phase was observed in the beginning of de-sodiation (upon charging to 3.55 V, see Figure 6a). Afterwards, it showed a solid-solution type behavior with minor changes in peak position. This means that the cubic phase was maintained, even upon charging to 4.2 V (see Figure 6b-b₂) and during the subsequent re-sodiation process, indicating the preference for a highly symmetric structure. When the ΔS_{conf} is decreased to 1.32 R or 0.82 R, a similar trend in unit-cell expansion/contraction to the conventional Mn-PW is observed (see Figure 6c-c₂, d-d₂ and Figure S7 and S8). Compared with Mn-PW, the main difference is that the degree of lattice expansion/contraction
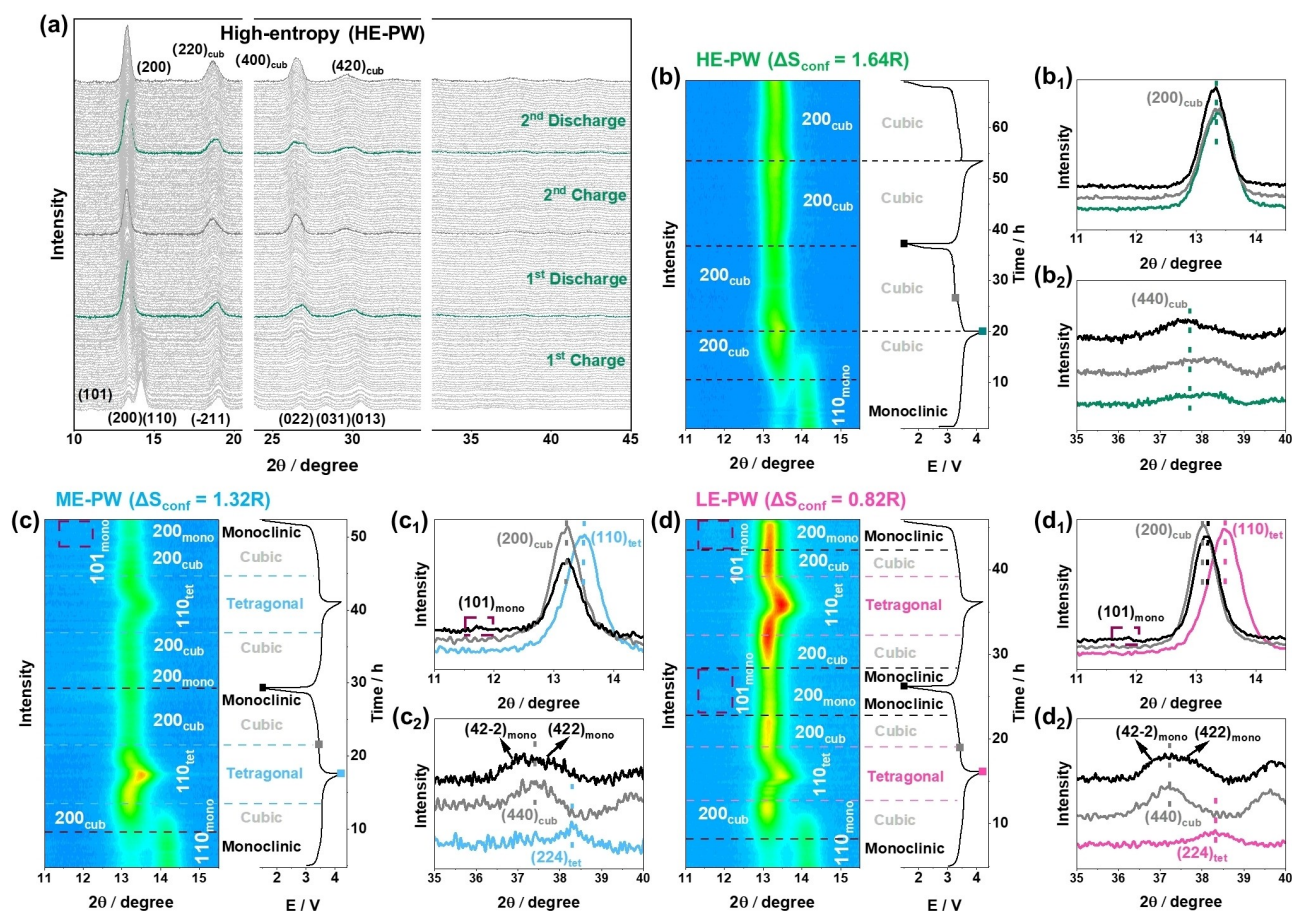
Figure 6. *Operando* XRD characterization of the HE-, ME- and LE-PW cathodes over the first two cycles. (a) Waterfall plot (scans between 10° to 45° 2-theta) for HE-PW. (b-d) Contour plots and corresponding voltage profiles for HE-, ME- and LE-PW. (b_1-d_1, b_2-d_2) XRD patterns collected at the end of first charge and during subsequent discharge [denoted by squares in the respective dis-/charge profiles in panels (b, c and d)].

was lower, as is evident from the XRD contour plots, suggesting that the structural evolution can be modulated to some extent by increasing the ΔS_{conf}. Particularly for ME-PW, the shift at high angles (growth of the tetragonal phase) was significantly smaller than for both LE- and Mn-PW. Consequently, the various phase transitions during electrochemical cycling seem to be responsible for the inferior performance of the LE- and Mn-PW cathodes. For a more detailed analysis, *ex situ* XRD measurements were conducted on the HE-PW and LE-PW cathodes (see Figure S9). While LE-PW showed a clear re-appearance of the monoclinic phase, the HE-PW was found to be present in the cubic form after a full battery cycle.

Overall, the *operando* XRD results demonstrate the benefits of the high-entropy approach for improving the PW stability. The larger the configurational entropy of the here presented systems, the stronger the suppression of phase changes to monoclinic and tetragonal (i.e., better maintaining structural symmetry and therefore stability). The trend observed in the structural degradation (Mn-PW > LE-PW > ME-PW > HE-PW) also accounts for the superior cycling performance of the materials with a higher ΔS_{conf} (see Figure 4).

To better understand the structural degradation of the PW materials, their gassing behavior was studied by DEMS.[61,62] In the following, the gas evolution of LE-PW and HE-PW is compared qualitatively and quantitatively. Figure 7 shows the gas evolution profiles of both materials in the second and third cycles for the most prominent gasses, while Figure S10 displays the whole measurement range. All quantifiable gas amounts are reported in Table S6. Hydrogen (H_2, $m/z = 2$) is evolved from the reduction of water and protic electrolyte degradation species at the anode. The observation of H_2 early into the first charge is therefore likely explained by the release of crystal water or coordinated water and coincides with the initial transition from monoclinic to cubic structure. It can be assumed that the phase transition is a driving force for the release of water due to structural rearrangement. This is especially evident when considering that the release of H_2 early into the charge is observed in the subsequent cycles and found to be much stronger for LE-PW, which, as discussed above, undergoes a corresponding transition from monoclinic to cubic phase. At the same time, much lower H_2 evolution was observed for HE-PW, even though both materials were dried under the same conditions and found to contain a similar amount of water, as reported in Table S3. Of note is that no concurrent

Angew. Chem. Int. Ed. **2023**, e202315371 (9 of 14)

© 2023 The Authors. Angewandte Chemie International Edition published by Wiley-VCH GmbH
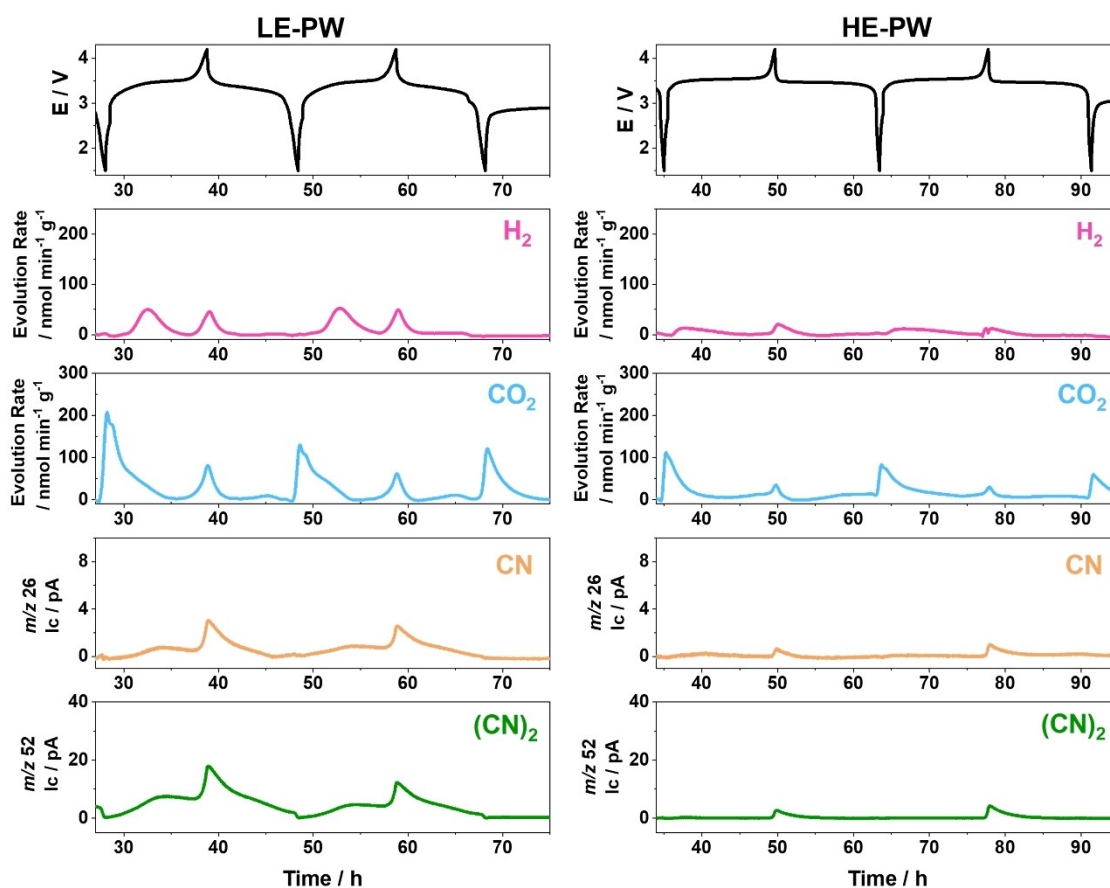
Figure 7. *In situ* gas analysis. Gas evolution profiles for the LE-PW and HE-PW cathodes as obtained via DEMS.

carbon dioxide (CO_2, $m/z = 44$) evolution was observed during the early charge, which can be formed as a byproduct of ethylene carbonate hydrolysis.[63] At high potentials and state of charge (SOC), H_2 evolution is increasing as coordinated water is released in the form of $Na(OH_2)^+$, due to reduced binding energy.[64,65]

CO_2 is evolved from the electrochemical electrolyte oxidation and/or degradation of surface impurities, such as carbonates, which were recently shown to also be present in PWs.[66–68] The higher amount of CO_2 in the first cycle is likely due to these surface impurities, since their decomposition is largely limited to the first cycle,[67] while the rather similar gas amounts between the second and third cycle indicates a recurring reaction. The gas evolution was again stronger for LE-PW, although the specific capacity and SOC were higher for HE-PW. Because of the slightly different shape of the voltage profiles, it may be argued that the higher gas evolution is solely due to the longer time spent at high potentials. For this reason, the gas evolution rate as a function of potential is shown in Figure S11, demonstrating that for any given potential, the CO_2 evolution rate is higher for LE-PW than for HE-PW. Additional CO_2 evolution, but no H_2 evolution, was observed during the end of discharge at potentials below 1.8 V. As reported previously for P2-type layered oxide SIB materials, this is likely due to the reduction of fluoro-

ethylene carbonate at the cathode side, which is known to release CO_2, but no H_2, at low potentials.[11,69]

Finally, cyanogen gas [$(CN)_2$] was detected both at $m/z = 52$ and 26, but no hydrogen cyanide (HCN, $m/z = 27$), which was also found previously.[16] While the release of $(CN)_2$ is known to occur during thermal decomposition of PW/PBA cathodes,[70,71] here electrochemical decomposition is occurring. In lack of a calibration gas mixture, absolute detector currents are reported, which are higher in this work due to changes discussed in the Methods section. However, as shown for the $m/z = 2$ signal (see Figure S12), the absolute signal intensity was similar between both materials, as they were measured in direct succession without changes in parameters and baseline values and with electrodes of same active material content. Hence, the $m/z = 52$ and 26 signals can be considered proportional to the $(CN)_2$ evolution rate. A drastic difference was observed between curve shape and evolution signal for LE-PW and HE-PW. In LE-PW, the $(CN)_2$ evolution rate showed a strong recurring shoulder (albeit of decreasing intensity) during each early charge, coinciding with the H_2 evolution, already attributed to the transition from monoclinic to cubic phase. Overall, it appears that phase transitions are at the root of another degradation mechanism, namely the release of $(CN)_2$ from the active material. Also, both materials showed $(CN)_2$ evolution at high potentials near the end of charge, yet again
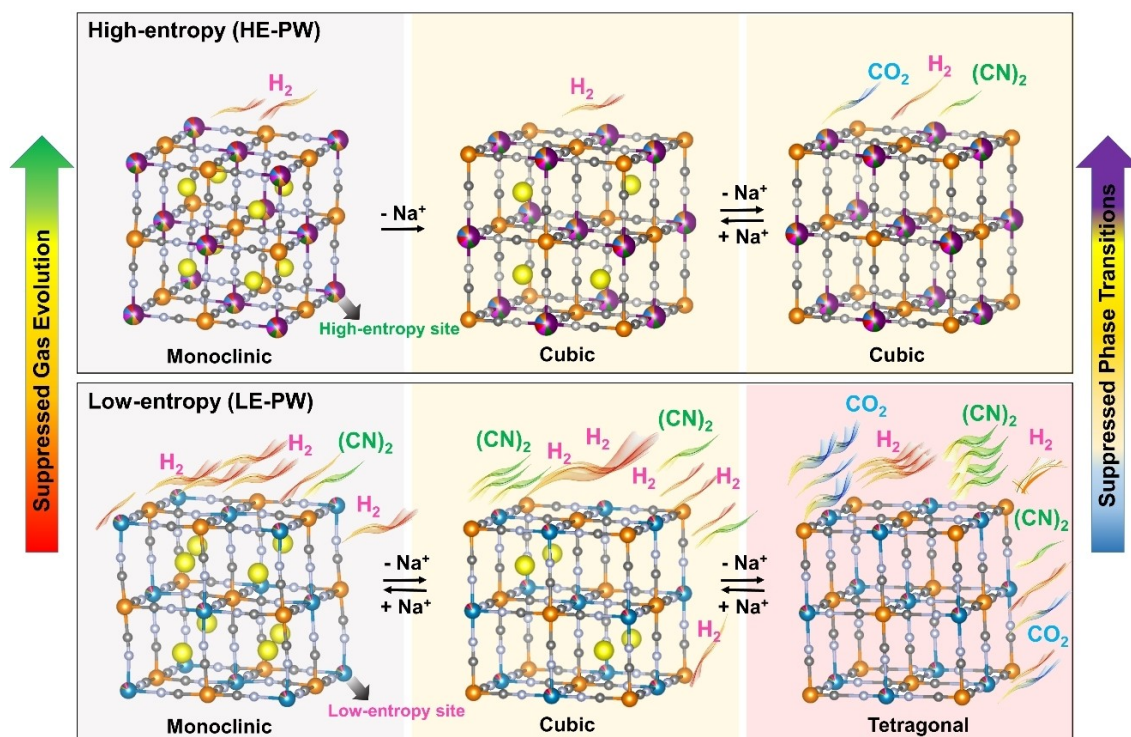
Figure 8. Schematic illustration of the structural evolutions and corresponding gassing behavior of HE-PW and LE-PW.

the interpolated evolution rate at any given potential was much higher for LE-PW than for HE-PW (see Figure S13). Interestingly, in Figure S13, a small shoulder of $(CN)_2$ evolution around 3.5 V is also visible for the HE-PW. Previously, the release of $(CN)_2$ at high potentials and SOC was reported as being analogous to the release of O_2 from layered oxides,[66,72] with both adhering to the abstract concept of oxidative dimerization of host structure anions.[16] The evolution of $(CN)_2$ at low SOC requires a reconsideration of this analogy, as it is not observed for lattice oxygen. However, for layered oxides, another considerable source of gas evolution are surface carbonates.[62,67] These may decompose to CO_2 either chemically by acid protons or electrochemically by oxidation, forming both CO_2 and O_2. It should be noted though, that the contribution of each mechanism is disputed.[62,73–75] Considering an analogy to this electrochemical oxidation, the oxidation of surface cyanide species, such as NaCN or $Na_4[Fe(CN)_6]$,[76] may contribute to the $(CN)_2$ evolution. Repeated phase transitions, leading to particle fracture and exposure of fresh surfaces, may then explain the gas evolution in the following cycles. A further DEMS investigation into crack formation, surface reactions and $(CN)_2$ quantification is underway but outside the scope of this work.

Taken together, the concurrent evolution of H_2 and $(CN)_2$ already at the beginning of charge is strong evidence for the detrimental role of phase transitions, as the structural rearrangement triggers gas-evolving degradation reactions. The structural evolutions obtained from *operando* XRD and DEMS are summarized in Figure 8. As was shown, the high-entropy approach enables the preparation of a PW material

with largely suppressed gas evolution and phase transitions and therefore is an effective optimization measure.

Finally, first-principle DFT calculations were performed for the HE-, ME- and LE-PW materials to derive the Gibbs free energy of the considered phases and understand the impact of configurational entropy on stability. The results are given in Table 1. For the fully de-sodiated state, the cubic (*Fm*-3*m* space group) and tetragonal (*I*-4*m*2 space group) structures were considered and compared. Our results indicate that upon full extraction of Na^+ ions from the lattice ($Na_xTM[Fe(CN)_6]$ with $x=0$), HE-PW exists in the high-symmetry, cubic phase, whereas both ME-PW and LE-PW adopt a tetragonal structure that is thermodynamically more stable (see Figure 9a). This finding is in good

Table 1: The computed thermodynamic parameters for the HE-, ME- and LE-PW materials (for different degrees of sodiation, i.e., x in $Na_xTM[Fe(CN)_6]$). For $x=0$, the enthalpy difference between the cubic and tetragonal phases is presented. For $x=1$, the formation enthalpy, the configurational entropy contribution to the Gibbs free energy at 298 K and the Gibbs free energy of formation are reported (given in units of kJ mol^{-1}). For $x=1.5$, the enthalpy difference between the cubic and monoclinic phase in HE-PW is given.

	Energy	HE-PW	ME-PW	LE-PW
$x=0$	$\Delta H = H_{cubic} - H_{tet}$	−171.165	9.070	33.191
	ΔH_f	−403.018	−403.790	−404.369
$x=1$	$-T\Delta S_{conf}$ at 25 °C	−4.130	−3.345	−2.099
	$\Delta G_f = \Delta H_f - T\Delta S_{conf}$	−407.148	−407.135	−406.467
$x=1.5$	$\Delta H = H_{cubic} - H_{mono}$	−13.351	–	–
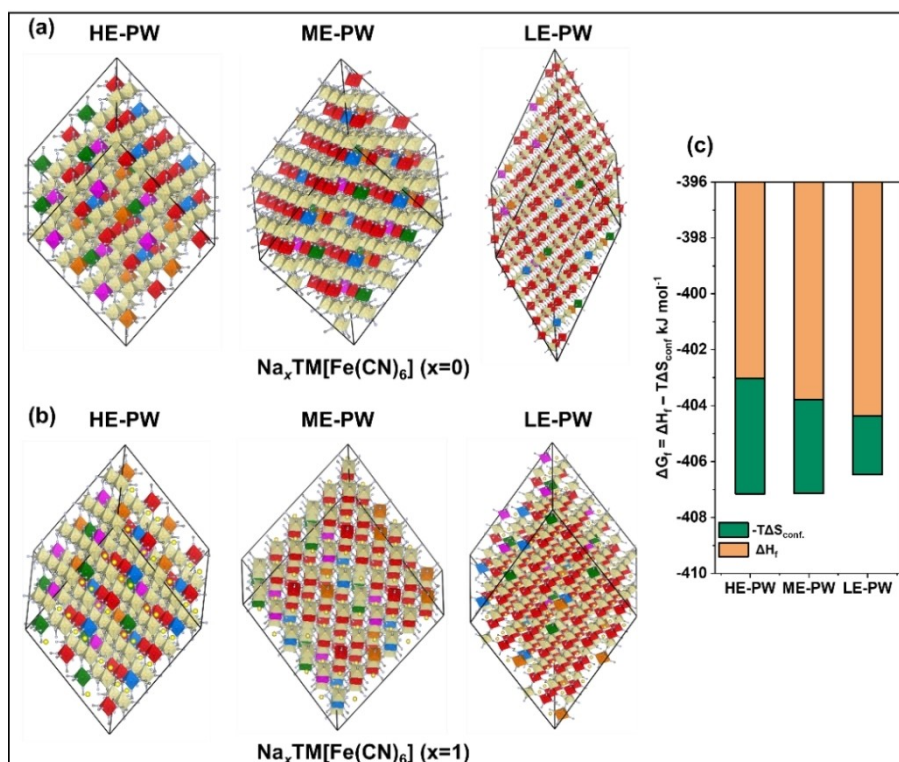
Figure 9. Crystal structures of (a) HE-PW (cubic), ME-PW (tetragonal) and LE-PW (tetragonal) in the fully charged state ($x=0$ in $Na_xTM[Fe(CN)_6]$). (b) Corresponding structures for $x=1$ (cubic). (c) The Gibbs free energy of formation of the three systems at 298 K.

agreement with the XRD results and validates the experimentally observed phase transitions upon charging.

In the sodiated state ($x=1$), the cubic phase is most stable for all three materials. To compare the stability, their Gibbs free energies of formation (ΔG_f) were calculated. Although the formation enthalpy (ΔH_f) of LE-PW is lower by ≈ 1.4 and $\approx 0.6\ kJ\,mol^{-1}$ (more negative) than that of HE-PW and ME-PW, respectively, the difference can be readily overcome by the entropy term ($-T\Delta S_{conf}$) at room temperature (see Figure 9b), indicating some stabilization due to configurational entropy for HE-PW. As a result, the overall Gibbs free energies of formation at room temperature for HE-, ME- and LE-PW (sodiated state) are similar (within $1\ kJ\,mol^{-1}$), with the structural stability sequence of LE-PW < ME-PW < HE-PW.

In the highly sodiated state ($x=1.5$), which approximates the as-synthesized composition, the structural stability of the cubic and monoclinic phases was examined for HE-PW. The latter material exhibited a consistent pattern of structural stabilization in response to electrochemical cycling. The DFT result demonstrates that, for $x=1.5$, the cubic structure displays a greater stability than its monoclinic counterpart, as evidenced by a lower energy state (by about $-13.35\ kJ\,mol^{-1}$). A potential explanation for the synthesis of monoclinic HE-PW is kinetics. Thermodynamic principles dictate that a system tends to move toward its most stable state, i.e., the state with the lowest energy. However, kinetics can prevent the system from reaching this state. If the energy barrier between the monoclinic and cubic phase is

high, the system may remain trapped in the monoclinic phase, even though the cubic one is energetically more favorable. This phenomenon is often denoted as kinetic stabilization or kinetic trapping. In other words, although the cubic phase is more stable in terms of energy, as determined by DFT, the transition could be energetically prohibitive. The system may not have enough thermal energy to overcome the energy barrier and therefore is trapped in a metastable, monoclinic phase. However, during cycling, the input of external energy facilitates the phase transition, allowing the system to attain and maintain the more stable cubic phase. DFT-calculated structural parameters for the HE-, ME-, and LE-PW materials are given in Table S7. The computational results indicate that compositional disorder enables a more robust structure for accommodating the electrochemical reactions, and the preference for the high-symmetry structure of HE-PW was confirmed. This agrees well with the experimental data described above and highlights the importance of configurational entropy for increasing the stability of the materials. Last but not least, the mean voltages computed on the most stable structures (see Table S8) were found to match well with the electrochemical measurements.

Conclusion

In this work, the application of the high-entropy concept to Prussian White (PW) materials was evaluated by studying a

series of Mn-based, monoclinic PW cathodes composed of up to six transition metals on the Mn site. The six-metal high-entropy PW having a ΔS_{conf} of 1.64 R exhibits superior sodium-storage properties over medium-entropy ($\Delta S_{conf}=$ 1.32 R), low-entropy ($\Delta S_{conf}=0.82$ R) and conventional Mn-PW ($\Delta S_{conf}=0$ R) materials. The mechanism of this improved performance was investigated, and it was found that the introduction of compositional disorder can suppress unfavorable phase transitions and also reduce side reactions that lead to gas evolution during cycling. Through a series of complementary experiments and simulation studies, we demonstrate the positive effect that entropy increase has on the structural evolution and electrochemical behavior and, for the first time, confirm the preference for a high-symmetry structure upon battery operation. The unveiling of the mechanism behind the improved cycling performance and stability resulting from the introduction of high configurational entropy may provide a reference for future battery materials design.

Supporting Information

Methods and results from XRD, ICP-OES, TGA, synchrotron transmission XAFS, EDS mapping, XPS, CV, DEMS and DFT calculations, as well as structural and compositional information on the as-prepared samples.

Acknowledgements

Conflict of Interest

The authors declare no conflict of interest.

Data Availability Statement

The data that support the findings of this study are available in the supplementary material of this article.

Keywords: High-Entropy Materials · Outgassing · Phase Transitions · Prussian White · Sodium-Ion Cathode

[1] E. P. George, D. Raabe, R. O. Ritchie, *Nat. Rev. Mater.* **2019**, *4*, 515–534.

[2] C. Oses, C. Toher, S. Curtarolo, *Nat. Rev. Mater.* **2020**, *5*, 295–309.

[3] M. C. Gao, D. B. Miracle, D. Maurice, X. Yan, Y. Zhang, J. A. Hawk, *J. Mater. Res.* **2018**, *33*, 3138–3155.

[4] X. Shi, J. Zou, Z. Chen, *Chem. Rev.* **2020**, *120*, 7399–7515.

[5] X. Wang, W. Guo, Y. Fu, *J. Mater. Chem. A* **2021**, *9*, 663–701.

[6] Y. Ma, Y. Ma, Q. Wang, S. Schweidler, M. Botros, T. Fu, H. Hahn, T. Brezesinski, B. Breitung, *Energy Environ. Sci.* **2021**, *14*, 2883–2905.

[7] A. Amiri, R. Shahbazian-Yassar, *J. Mater. Chem. A* **2021**, *9*, 782–823.

[8] Q. Wang, A. Sarkar, D. Wang, L. Velasco, R. Azmi, S. S. Bhattacharya, T. Bergfeldt, A. Düvel, P. Heitjans, T. Brezesinski, H. Hahn, B. Breitung, *Energy Environ. Sci.* **2019**, *12*, 2433–2442.

[9] Z. Lun, B. Ouyang, D. H. Kwon, Y. Ha, E. E. Foley, T. Y. Huang, Z. Cai, H. Kim, M. Balasubramanian, Y. Sun, J. Huang, Y. Tian, H. Kim, B. D. McCloskey, W. Yang, R. J. Clément, H. Ji, G. Ceder, *Nat. Mater.* **2021**, *20*, 214–221.

[10] A. Sarkar, L. Velasco, D. Wang, Q. Wang, G. Talasila, L. de Biasi, C. Kübel, T. Brezesinski, S. S. Bhattacharya, H. Hahn, B. Breitung, *Nat. Commun.* **2018**, *9*, 3400.

[11] J. Wang, S. L. Dreyer, K. Wang, Z. Ding, T. Diemant, G. Karkera, Y. Ma, A. Sarkar, B. Zhou, M. V Gorbunov, A. Omar, D. Mikhailova, V. Presser, M. Fichtner, H. Hahn, T. Brezesinski, B. Breitung, Q. Wang, *Mater. Futures* **2022**, *1*, 035104.

[12] R. Zhang, C. Wang, P. Zou, R. Lin, L. Ma, L. Yin, T. Li, W. Xu, H. Jia, Q. Li, S. Sainio, K. Kisslinger, S. E. Trask, S. N. Ehrlich, Y. Yang, A. M. Kiss, M. Ge, B. J. Polzin, S. J. Lee, W. Xu, Y. Ren, H. L. Xin, *Nature* **2022**, *610*, 67–73.

[13] C. Zhao, F. Ding, Y. Lu, L. Chen, Y. S. Hu, *Angew. Chem. Int. Ed.* **2020**, *59*, 264–269.

[14] F. Fu, X. Liu, X. Fu, H. Chen, L. Huang, J. Fan, J. Le, Q. Wang, W. Yang, Y. Ren, K. Amine, S.-G. Sun, G.-L. Xu, *Nat. Commun.* **2022**, *13*, 2826.

[15] F. Ding, C. Zhao, D. Xiao, X. Rong, H. Wang, Y. Li, Y. Yang, Y. Lu, Y. Hu, *J. Am. Chem. Soc.* **2022**, *144*, 8286–8295.

[16] Y. Ma, Y. Ma, S. L. Dreyer, Q. Wang, K. Wang, D. Goonetilleke, A. Omar, D. Mikhailova, H. Hahn, B. Breitung, T. Brezesinski, *Adv. Mater.* **2021**, *33*, 2101342.

[17] Y. Ma, Y. Hu, Y. Pramudya, T. Diemant, Q. Wang, D. Goonetilleke, Y. Tang, B. Zhou, H. Hahn, W. Wenzel, M. Fichtner, Y. Ma, B. Breitung, T. Brezesinski, *Adv. Funct. Mater.* **2022**, *32*, 2202372.

[18] J. Peng, B. Zhang, W. Hua, Y. Liang, W. Zhang, Y. Du, G. Peleckis, S. Indris, Q. Gu, Z. Cheng, J. Wang, H. Liu, S. Dou, S. Chou, *Angew. Chem. Int. Ed.* **2023**, *62*, e202215865.

[19] Y. Ma, T. Brezesinski, B. Breitung, Y. Ma, *Matter* **2023**, *6*, 313–315.

[20] X. Zhao, Z. Xing, C. Huang, *J. Mater. Chem. A* **2023**, *20*, 22835–22844.

[21] J. Dai, S. Tan, L. Wang, F. Ling, F. Duan, M. Ma, Y. Shao, X. Rui, Y. Yao, E. Hu, X. Wu, C. Li, Y. Yu, *ACS Nano* **2023**, *17*, 20949–20961.

[22] J. Peng, W. Zhang, Q. Liu, J. Wang, S. Chou, H. Liu, S. Dou, *Adv. Mater.* **2022**, *34*, 2108384.

[23] J. Qian, C. Wu, Y. Cao, Z. Ma, Y. Huang, X. Ai, H. Yang, *Adv. Energy Mater.* **2018**, *8*, 1702619.

[24] Q. Liu, Z. Hu, M. Chen, C. Zou, H. Jin, S. Wang, S. L. Chou, Y. Liu, S. X. Dou, *Adv. Funct. Mater.* **2020**, *30*, 1909530.

Angew. Chem. Int. Ed. **2023**, e202315371 (13 of 14)

© 2023 The Authors. Angewandte Chemie International Edition published by Wiley-VCH GmbH

[25] W. Li, C. Han, W. Wang, Q. Xia, S. Chou, Q. Gu, B. Johannessen, H. K. Liu, S. Dou, *Adv. Energy Mater.* **2020**, *10*, 1903006.

[26] L. Wang, J. Song, R. Qiao, L. A. Wray, M. A. Hossain, Y. De Chuang, W. Yang, Y. Lu, D. Evans, J. J. Lee, S. Vail, X. Zhao, M. Nishijima, S. Kakimoto, J. B. Goodenough, *J. Am. Chem. Soc.* **2015**, *137*, 2548–2554.

[27] Y. Shang, X. Li, J. Song, S. Huang, Z. Yang, Z. J. Xu, H. Y. Yang, *Chem* **2020**, *6*, 1804–1818.

[28] V. Renman, D. O. Ojwang, C. Pay Gómez, T. Gustafsson, K. Edström, G. Svensson, M. Valvo, *J. Phys. Chem. C* **2019**, *123*, 22040–22049.

[29] K. Hurlbutt, S. Wheeler, I. Capone, M. Pasta, *Joule* **2018**, *2*, 1950–1960.

[30] X. Huang, C. Yang, Y. You, *ACS Appl. Energ. Mater.* **2022**, *5*, 8123–8131.

[31] L. Jiang, Y. Lu, C. Zhao, L. Liu, J. Zhang, Q. Zhang, X. Shen, J. Zhao, X. Yu, H. Li, X. Huang, L. Chen, Y. S. Hu, *Nat. Energy* **2019**, *4*, 495–503.

[32] D. Yang, J. Xu, X. Liao, Y. He, H. Liu, Z. Ma, *Chem. Commun.* **2014**, *50*, 13377–13380.

[33] J. Zhang, J. Wan, M. Ou, S. Liu, B. Huang, J. Xu, S. Sun, Y. Xu, *Energy Mater.* **2023**, *3*, 300008.

[34] Y. You, X. L. Wu, Y. X. Yin, Y. G. Guo, *Energy Environ. Sci.* **2014**, *7*, 1643–1647.

[35] J. Song, L. Wang, Y. Lu, J. Liu, B. Guo, P. Xiao, J. J. Lee, X. Q. Yang, G. Henkelman, J. B. Goodenough, *J. Am. Chem. Soc.* **2015**, *137*, 2658–2664.

[36] Y. Xu, J. Wan, L. Huang, M. Ou, C. Fan, P. Wei, J. Peng, Y. Liu, Y. Qiu, X. Sun, C. Fang, Q. Li, J. Han, Y. Huang, J. A. Alonso, Y. Zhao, *Adv. Energy Mater.* **2019**, *9*, 1803158.

[37] Y. Tang, W. Li, P. Feng, M. Zhou, K. Wang, Y. Wang, K. Zaghib, K. Jiang, *Adv. Funct. Mater.* **2020**, *30*, 1908754.

[38] L. Deng, J. Qu, X. Niu, J. Liu, J. Zhang, Y. Hong, M. Feng, J. Wang, M. Hu, L. Zeng, Q. Zhang, L. Guo, Y. Zhu, *Nat. Commun.* **2021**, *12*, 2167.

[39] Y. You, H. Yao, S. Xin, Y. Yin, T. Zuo, C. Yang, Y. Guo, Y. Cui, L. Wan, J. B. Goodenough, *Adv. Mater.* **2016**, *28*, 7243–7248.

[40] W.-J. Li, S.-L. Chou, J.-Z. Wang, J.-L. Wang, Q.-F. Gu, H.-K. Liu, S.-X. Dou, *Nano Energy* **2015**, *13*, 200–207.

[41] M. Oliver-Tolentino, M. González, H. Osiry, G. Ramos-Sánchez, I. González, *Dalton Trans.* **2018**, *47*, 16492–16501.

[42] F. M. Maddar, D. Walker, T. W. Chamberlain, J. Compton, A. S. Menon, M. Copley, I. Hasa, *J. Mater. Chem. A* **2023**, *11*, 15778–15791.

[43] W. Wang, Y. Gang, J. Peng, Z. Hu, Z. Yan, W. Lai, Y. Zhu, D. Appadoo, M. Ye, Y. Cao, Q. Gu, H. Liu, S. Dou, S. Chou, *Adv. Funct. Mater.* **2022**, *32*, 2111727.

[44] L. Hartmann, J. Deshmukh, L. Zhang, S. Buechele, M. Metzger, *J. Electrochem. Soc.* **2023**, *170*, 030540.

[45] B. S. Murty, J.-W. Yeh, R. Srikanth, P. P. Bhattacharjee, *High-Entropy Alloys*, Elsevier, Amsterdam, **2019**.

[46] M. Giorgetti, M. Berrettoni, *Inorg. Chem.* **2008**, *47*, 6001–6008.

[47] D. Jiang, Z. Sun, H. Jia, D. Lu, P. Du, *J. Mater. Chem. A* **2016**, *4*, 675–683.

[48] Z. Yan, X. Yu, A. Han, P. Xu, P. Du, *J. Phys. Chem. C* **2014**, *118*, 22896–22903.

[49] X. Zhang, M. Xia, T. Liu, N. Peng, H. Yu, R. Zheng, L. Zhang, M. Shui, J. Shu, *Chem. Eng. J.* **2021**, *421*, 127767.

[50] M. C. Biesinger, B. P. Payne, A. P. Grosvenor, L. W. M. Lau, A. R. Gerson, R. S. C. Smart, *Appl. Surf. Sci.* **2011**, *257*, 2717–2730.

[51] I. Sarhid, I. Lampre, D. Dragoe, P. Beaunier, B. Palpant, H. Remita, *Materials* **2019**, *12*, 3012.

[52] M. Giorgetti, S. Della Longa, M. Benfatto, *J. Phys. Conf. Ser.* **2009**, *190*, 012145.

[53] M. Giorgetti, L. Guadagnini, D. Tonelli, M. Minicucci, G. Aquilanti, *Phys. Chem. Chem. Phys.* **2012**, *14*, 5527.

[54] J. Sottmann, F. L. M. Bernal, K. V. Yusenko, M. Herrmann, H. Emerich, D. S. Wragg, S. Margadonna, *Electrochim. Acta* **2016**, *200*, 305–313.

[55] S. Lafuerza, A. Carlantuono, M. Retegan, P. Glatzel, *Inorg. Chem.* **2020**, *59*, 12518–12535.

[56] C. J. Pollock, M. U. Delgado-Jaime, M. Atanasov, F. Neese, S. Debeer, *J. Am. Chem. Soc.* **2014**, *136*, 9453–9463.

[57] G. Peng, F. M. F. DeGroot, K. Hämáláinen, J. A. Moore, X. Wang, M. M. Crush, J. B. Hastings, D. P. Siddons, W. H. Armstrong, O. C. Mullins, S. P. Cramer, *J. Am. Chem. Soc.* **1994**, *116*, 2914–2920.

[58] U. Bergmann, M. M. Grush, C. R. Horne, P. Demarois, C. F. Yocum, D. W. Wright, C. E. Dube, W. H. Armstrong, G. Christou, H. J. Eppley, S. P. Cramer, *J. Phys. Chem. B* **1998**, *102*, 8350–8352.

[59] M. A. Beckwith, M. Roemelt, C. Duboc, T. Weng, U. Bergmann, P. Glatzel, F. Neese, S. Debeer, *Inorg. Chem.* **2011**, *50*, 8397–8409.

[60] W. Wang, Y. Gang, Z. Hu, Z. Yan, W. Li, Y. Li, Q.-F. Gu, Z. Wang, S.-L. Chou, H.-K. Liu, S.-X. Dou, *Nat. Commun.* **2020**, *11*, 980.

[61] B. Rowden, N. Garcia-Araez, *Energy Rep.* **2020**, *6*, 10–18.

[62] S. L. Dreyer, A. Kondrakov, J. Janek, T. Brezesinski, *J. Mater. Res.* **2022**, *37*, 3146–3168.

[63] M. Metzger, B. Strehle, S. Solchenbach, H. A. Gasteiger, *J. Electrochem. Soc.* **2016**, *163*, A1219-A1225.

[64] Y. Yang, E. Liu, X. Yan, C. Ma, W. Wen, X.-Z. Liao, Z.-F. Ma, *J. Electrochem. Soc.* **2016**, *163*, A2117-A2123.

[65] S. G. Patnaik, P. Adelhelm, *Sodium-Ion Batteries* Wiley-VCH, Weinheim, **2022**, pp. 167–187.

[66] R. Jung, M. Metzger, F. Maglia, C. Stinner, H. A. Gasteiger, *J. Phys. Chem. Lett.* **2017**, *8*, 4820–4825.

[67] T. Hatsukade, A. Schiele, P. Hartmann, T. Brezesinski, J. Janek, *ACS Appl. Mater. Interfaces* **2018**, *10*, 38892–38899.

[68] M. Metzger, B. Strehle, S. Solchenbach, H. A. Gasteiger, *J. Electrochem. Soc.* **2016**, *163*, A798-A809.

[69] K. U. Schwenke, S. Solchenbach, J. Demeaux, B. L. Lucht, H. A. Gasteiger, *J. Electrochem. Soc.* **2019**, *166*, A2035-A2047.

[70] Z. Li, M. Dadsetan, J. Gao, S. Zhang, L. Cai, A. Naseri, M. E. Jimenez-Castaneda, T. Filley, J. T. Miller, M. J. Thomson, V. G. Pol, *Adv. Energy Mater.* **2021**, *11*, 2101764.

[71] D. O. Ojwang, L. Häggström, T. Ericsson, J. Ångström, W. R. Brant, *Dalton Trans.* **2020**, *49*, 3570–3579.

[72] D. Streich, C. Erk, A. Guéguen, P. Müller, F. Chesneau, E. J. Berg, *J. Phys. Chem.* **2017**, *121*, 13481–13486.

[73] A. T. S. Freiberg, J. Sicklinger, S. Solchenbach, H. A. Gasteiger, *Electrochim. Acta* **2020**, *346*, 136271.

[74] L. A. Kaufman, B. D. McCloskey, *Chem. Mater.* **2021**, *33*, 4170–4176.

[75] F. Strauss, S. Payandeh, A. Kondrakov, T. Brezesinski, *Mater. Futures* **2022**, *1*, 023501.

[76] D. O. Ojwang, M. Svensson, C. Njel, R. Mogensen, A. S. Menon, T. Ericsson, L. Häggström, J. Maibach, W. R. Brant, *ACS Appl. Mater. Interfaces* **2021**, *13*, 10054–10063.

Research Articles

Batteries

Y. He, S. L. Dreyer, Y.-Y. Ting, Y. Ma, Y. Hu,
D. Goonetilleke, Y. Tang, T. Diemant,
B. Zhou, P. M. Kowalski, M. Fichtner,
H. Hahn, J. Aghassi-Hagmann,
T. Brezesinski,* B. Breitung,*
Y. Ma* —————————— e202315371

Entropy-Mediated Stable Structural Evolu-
tion of Prussian White Cathodes for Long-
Life Na-Ion Batteries
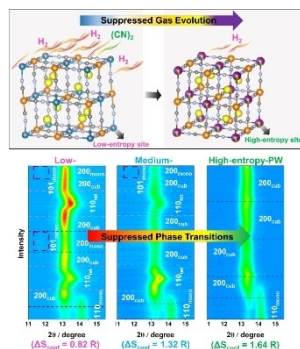
The high-entropy approach is applied to a monoclinic Prussian White (PW), yielding a promising cathode material $(Na_{1.65}Mn_{0.4}Fe_{0.12}Ni_{0.12}Cu_{0.12}Co_{0.12}Cd_{0.12}[Fe(CN)_6]_{0.92}\square_{0.08} \cdot 1.09H_2O)$ for Na-ion battery applications. Comparison of the structural and chemical properties of high-, medium- and low-entropy Mn-based PWs reveals the performance benefits arising from increased configurational entropy, namely suppression of phase transitions and mitigation of gas evolution during cycling.